Simultaneous Magnetic Resonance Wireless Power and High-Speed Data Transfer System With Cascaded Equalizer for Variable Channel Compensation

Li Wang, *Student Member, IEEE*, Xianbo Li, *Member, IEEE*, Salahuddin Raju, *Member, IEEE*, and C. Patrick Yue, *Fellow, IEEE*

***Abstract*—Wireless power transfer (WPT) systems can potentially provide simultaneous power and data transfer for Internet-of-Things devices, such as smart speakers, glasses, and watches. However, due to the high quality factor of coils, the intrinsically narrow WPT channel bandwidth severely limits the data transmission capability of the system, especially for data downloading links requiring higher data rates. In addition, the channel bandwidth varies with power transfer distances, which is also undesirable for wireless communication. In this study, the channel features of a two-coil series–series matching magnetic resonance wireless power and data transfer (MWPDT) system, including the bandwidth and the roll-off slope are characterized analytically. Based on the characterization results, a receiver front-end circuit with a three-stage cascaded equalizer (EQ) is proposed and implemented to extend the bandwidth of a MWPDT system at different distances. The proposed EQ can provide a frequency response with a variable roll-up slope from 10 to 45 dB/dec to compensate for the distance-dependent channel response of an MWPDT system. A complete MWPDT system is built and tested to verify the performance of the proposed method. Experimental results demonstrate that the data rates can be extended from 650, 500, and 350 kbps to 850, 700, and 650 kbps at 0.4, 0.5, and 0.6-m distances, respectively. The highest data rate extension ratio is 85% at a transmission distance of 0.6 m, which is 2.4 times the radii of the coil employed in the system.**

***Index Terms*—Bandwidth, cascaded equalizer (EQ), magnetic resonance wireless power and data transfer (MWPDT), receiver, roll-up slope (ROS).**

Manuscript received January 13, 2019; revised March 28, 2019; accepted April 26, 2019. Date of publication May 9, 2019; date of current version September 6, 2019. This work was supported by the HKUST-Qualcomm Joint Innovation and Research Laboratory. Recommended for publication by Associate Editor J. Acero. *(Corresponding author: Xianbo Li.)*

The authors are with the Department of Electronic and Computer Engineering, Hong Kong University of Science and Technology, Hong Kong (e-mail: lwangbk@connect.ust.hk; xlibc@connect.ust.hk; rsalahuddin@connect.ust.hk; eepatrick@ust.hk).

This paper has supplementary downloadable material available at http://ieeexplore.ieee.org. This paper is accompanied by a video file demonstrating the bandwidth extension function of the EQ circuit. The size of the file is 8.19 MB. Contact lwangbk@connect.ust.hk for more information.

Color versions of one or more of the figures in this paper are available online at http://ieeexplore.ieee.org.

Digital Object Identifier 10.1109/TPEL.2019.2916021

I. Introduction

WIRELESS power transfer (WPT) technology has attracted wide research efforts since Tesla demonstrated the first WPT system prototype to power up a light bulb [1], [2]. Recently, with the ever-increasing demand for Internet-of-Things (IoT) devices, WPT technology is playing an important role in charging portable devices due to its high flexibility. Among the most popular WPT techniques, such as inductive coupled power transfer and capacitive coupled power transfer, magnetic resonance wireless power transfer (MWPT) technique achieves a good balance between operation distance and power transfer efficiency [3]. MWPT systems are capable of transmitting power from a few milliwatts to several kilowatts over distances from a few millimeters to more than one meter [4], [5]. Therefore, MWPT systems can provide reliable charging accesses for vehicles, smart portable devices, and implant devices [6]–[8].

The rapid growth in the number of IoT and portable devices not only challenges the existing charging systems, but also causes unprecedented pressure on wireless communication systems. Conventional radio frequency (RF) communication technology is lacking in spectrum resources and cannot provide enough communication accesses, especially under environments with a high density of users, such as airports and shopping malls. Since MWPT systems are essentially resonance tanks, the power transfer channels can potentially be used for simultaneous data transmission to support the communication function. As shown in Fig. 1, magnetic resonance wireless power and data transfer (MWPDT) technology can be implemented seamlessly with the rapidly developing power line communication (PLC) technology to provide simultaneous power and internet connections for IoT devices, such as smart speakers, glasses, and watches [9].

The critical problem in implementing MWPDT systems for IoT devices is the tradeoff between the high quality (Q) factor of the coils and data transmission bandwidth. With a larger coil inductance, and therefore higher Q factor, a longer transmission distance and a higher efficiency can be achieved, but at the cost of a narrower bandwidth. There have been significant research efforts focusing on developing novel MWPDT system architectures. In [10]–[15], power and data were transmitted using carrier

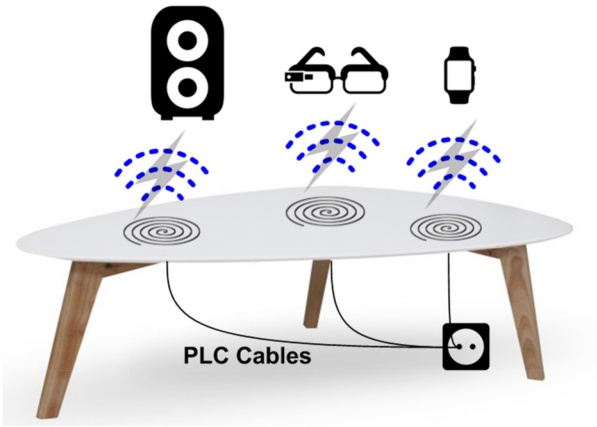

Fig. 1. Integrating MWPDT and PLC technology for simultaneous charging and communication of IoT devices.

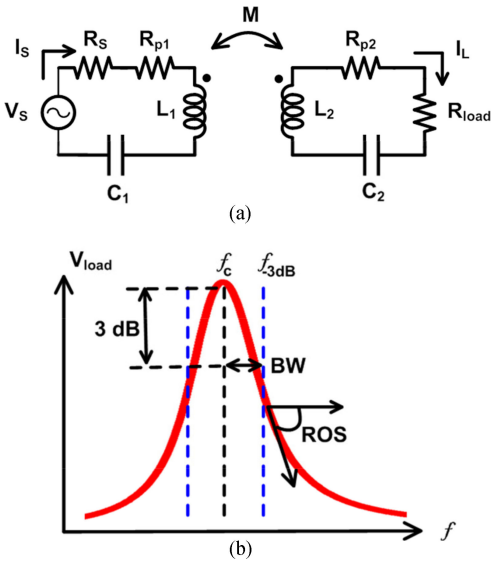

Fig. 2. (a) Circuit model of a typical two-coil s-s matching MWPT system. (b) Received voltage on the load resistor at different frequencies.

waves with separate frequencies to extend the data transmission bandwidth and reduce the cross talk. By centering the power and data carriers at lower and higher frequencies, respectively, data rates of 19.2 [10], [11], 20 [12], 100 [13], 119 [14], and 560 kbps [15] were achieved and the cross talk between power and data was suppressed. In [16] and [17], power and data were transmitted at two different pairs of coils with different resonance frequencies, which was suitable for short-distance biomedical applications. In [18], backward data transmission was achieved to send a control command from the receiver side to the transmitter side for vehicle charging and status monitoring. In [19], a novel system was proposed using trapezoidal current to transmit power and data simultaneously. The fundamental component of the trapezoidal current waveform was used to transfer power and its third-order harmonic component was selected to transmit information.

However, there still exist some challenges limiting the practical implementation of MWPDT systems. First, the method of separating power and data requires either multi-resonance structures or multi-coil systems, which increase the design complexity. Second, the problem of the intrinsically narrow channel bandwidth has not yet been solved. In addition, the channel features of a MWPDT system, such as bandwidth and roll-off slope (ROS), varies with operation distances, which results in an unstable communication channel undesirable for wireless communication.

In order to solve these problems, we propose a receiver front-end (RX) circuit with three-stage cascaded equalizer (EQ) to compensate for the limited bandwidth and the distance-dependent channel response of MWPDT systems. The cascaded EQ consists of two first-order EQ stages and one second-order EQ stage. It is capable of providing a variable compensation frequency (CF), a roll-up height (RUH), and a roll-up slope (RUS) from 10 to 45 dB/dec. A complete MWPDT system with a typical series–series matching two-coil structure is built to verify the circuit performance. Experimental results demonstrate that the highest data rate can be extended from 650, 500, and 350 kbps up to 850, 700, and 650 kbps at distances of 0.4, 0.5, and 0.6 m, respectively, with the received power as high as 2 W.

This paper is organized as follows. Section II theoretically characterizes the channel of a typical MWPDT system. The variation of bandwidth and out-of-band ROS at different transmission distances is analyzed. Section III describes the design and simulation of the proposed RX circuit with three-stage cascaded EQ. Section IV presents the complete MWPDT system, which consists of a two-coil structure and a power and data decoupling (PDD) circuit. Section V shows the experimental results. Finally, a conclusion is drawn in Section VI.

II. Channel Characterization of an MWPDT System

The channel bandwidth and out-of-band ROS of a typical two-coil MWPT system is characterized analytically to provide a guideline for the RX circuit design. Here, we consider the case when the data and power are transmitted via a shared channel and received simultaneously on a load. A series–series (s-s) matching MWPDT system is shown in Fig. 2(a). The system consists of a signal source V_s with a source impedance R_s, a load resistor R_{load}, a transmitting L_1, a receiving coils L_2, the coil parasitic resistances R_{p1}, R_{p2}, and two matching capacitors C_1,C_2. The center frequency f_c, at which maximum power transfer can be achieved on R_{load}, is determined by the resonance condition of L_1, C_1 and L_2, C_2 as follows:

$$f_c = \sqrt{\frac{1}{L_1 C_1}} = \sqrt{\frac{1}{L_2 C_2}}. \tag{1}$$

The received voltage across R_{load} (V_{load}) gradually decreases when the source signal frequency deviates from f_c. The frequency point when the received voltage across R_{load} reduces by 3 dB compared to the received voltage at f_c is denoted as $f_{-3\,dB}$, as shown in Fig. 2(b). The channel bandwidth (BW) is thus determined as follows:

$$\mathrm{BW} = |f_{-3\,\mathrm{dB}} - f_c|. \tag{2}$$

A transmitted signal can be successfully recovered on the receiver side when the Nyquist frequency of the signal falls within

BW. When the signal's Nyquist frequency goes outside BW, the intensity of the out-of-band spectrum component drops sharply so that the signal cannot be recovered properly. Out-of-band ROS describes how fast the frequency response of a MWPT system drops at frequencies outside the BW. As shown in Fig. 2(b), the ROS can be calculated using the following equation:

$$\mathrm{ROS} = \left| \frac{1}{V_s} \frac{\partial V_{\mathrm{load}}}{\partial f} \right|. \tag{3}$$

In order to calculate the BW and ROS, V_{load} at different frequencies needs to be analytically calculated. The circuit equations of Fig. 2(a) are shown as follows:

$$V_s = I_s \left(R_s + R_{p1} + j \left(2\pi f L_1 - \frac{1}{2\pi f C_1} \right) \right) + j2\pi f M I_L \tag{4}$$

$$0 = I_L \left(R_{\mathrm{load}} + R_{p2} + j \left(2\pi f L_2 - \frac{1}{2\pi f C_2} \right) \right) + j2\pi f M I_s. \tag{5}$$

The mutual inductance M can be calculated using coupling factor k with the following equation:

$$M = k\sqrt{L_1 L_2}. \tag{6}$$

Under the condition of symmetric transmitting and receiving coils with equal inductance L, equal source and load R, based on the (1) and (4)–(6), V_{load} can be calculated as in (7) shown at the bottom of this page.

V_{center} is also calculated as follows:

$$V_{\mathrm{center}} = \frac{-j2\pi f_c^3 kLR}{4\pi^2 f_c^4 k^2 L^2 + f_c^2 R^2}. \tag{8}$$

The design parameters of the MWPDT system are coil radii r, inductance L, and resonance frequency f_c, which are determined by application specifications. Other parameters such as matching capacitors C_1 and C_2 and coupling factor k can be calculated based on the design parameters. In our system, both the transmitting and receiving coil inductances are set to 30 μH, and the coil radii are set to 0.25 m. The resonance frequency f_c is set to 4.25 MHz. The R_s is 50 Ω considering the typical RF power amplifier (PA) output load. The parasitic resistances R_{p1} and R_{p2} are 14 and 7 Ω, respectively.

In the case that the two coils share the same radii r and are separated by a distance of d, their coupling factor can be calculated using the following equation when d is comparable to r [20], [21]:

$$k = \frac{1}{\left[1 + 2^{2/3}(d/r)^2\right]^{3/2}}. \tag{9}$$

The equation indicates that the ratio of the power transfer distance over the coil radii d/r is more meaningful and convenient for analysis.

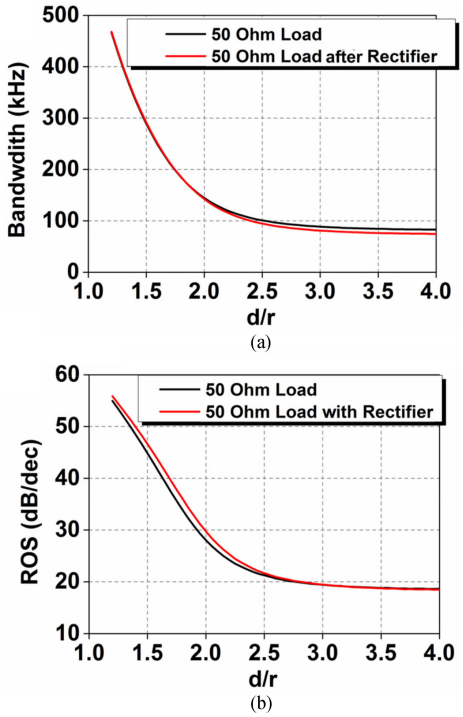

Fig. 3. (a) Calculated variation of BW versus d/r. (b) Calculated variation of ROS versus d/r.

The BW and out-of-band ROS can be calculated using (2), (3), and (7)–(9). The calculation is performed under two different loading conditions, a pure 50-Ω resistive load and a 50-Ω resistive load after a full-bridge rectifier. The latter loading condition is in accordance with our designed MWPDT system. The equivalent resistance of a 50-Ω load after a full-bridge rectifier with large filtering capacitor is 40.52 Ω [22]. The calculated BW and ROS versus d/r are presented in Fig. 3(a) and (b), respectively, which indicate that both ROS and BW drop with increased transmission distance. The ROS varies from 17 to 55 dB/dec when d/r increases from 1.2 to 4. The bandwidth drops to below 100 kHz when d/r is beyond 2.5. The reason why BW drops with distance can be explained using the equivalent impedance seeing on the transmitter side to the receiver side as follows:

$$Z_{\mathrm{eq}} = \frac{k^2 L_1 L_2 (2\pi f)^2}{R_{\mathrm{load}}}. \tag{10}$$

At longer distances, the coupling factor k is smaller and causes the equivalent impedance Z_{eq} to decrease. Therefore, the Q factor of the transmitter side resonant tank is larger, which leads to a narrower BW.

III. Design of RX Circuit

A. Operation Principle

To transmit data and power simultaneously through the MWPDT channel, the data signal can be modulated with a power

$$V_{\mathrm{load}} = \frac{-j2\pi f^3 kLR}{4\pi^2 f^4 k^2 L^2 + f^2 R^2 - 4\pi^2 L^2 (f^2 - f_c^2)^2 + j4\pi f RL (f^2 - f_c^2)} \tag{7}$$

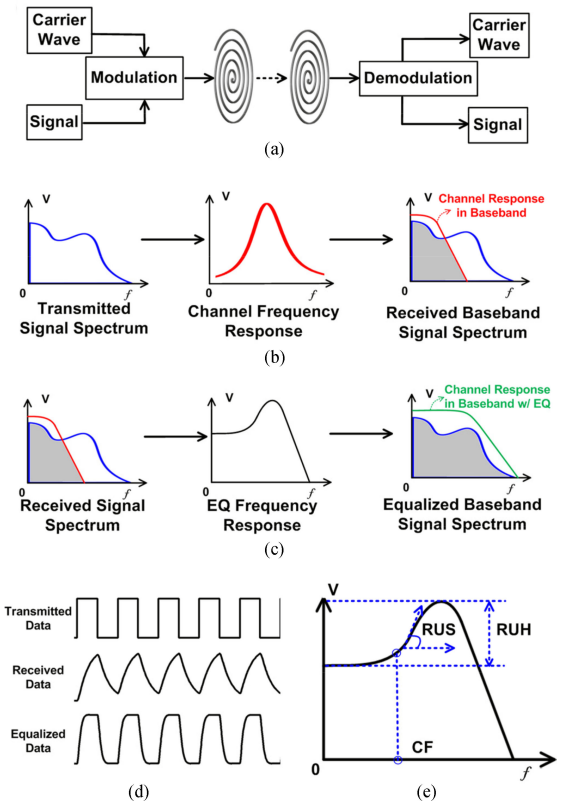

Fig. 4. (a) Block diagram of a MWPDT system. (b) Evolution of a signal spectrum when transmitted through the MWPDT system. (c) Principle of using an EQ circuit to extend the channel bandwidth and recover the original signal spectrum. (d) Evolution of the baseband data signal dynamic behavior when transmitted through the MWPDT system. (e) Definition of CF, RUS, and RUH of an EQ circuit.

carrier centered at f_c and transmitted through the matched coils. On the receiver side, the data signal and carrier wave are separated as shown in Fig. 4(a). Compared to transmitting data and power using separate carriers, this method requires no extra carrier for data transmission and is suitable for middle-range IoT devices charging and communication. However, when transmitting a high-speed data signal with wide baseband spectrum occupation, as shown with the blue curve in Fig. 4(b), the demodulated signal is low-pass filtered due to the narrow channel BW. Only the signal spectrum component shown by the gray area is left as indicated in Fig. 4(b). In order to recover the original signal spectrum properly, an EQ circuit with a high-pass frequency response shown with the black curve in Fig. 4(c) needs to be implemented to compensate for the frequency response roll-off of the MWPDT channel. The overall channel frequency response with the EQ circuit is shown with the green curve and the equalized signal spectrum is shown in the gray area in Fig. 4(c). Considering transmitting a periodic square wave as a data signal, the evolution of the dynamic behavior of the signal in baseband during the transmission and equalization process is shown in Fig. 4(d). The low-pass frequency response of the MWPDT channel suppress the signal high-frequency spectrum components and results in slow rising and falling edges, which can be compensated and recovered by using an EQ circuit with high-pass response.

Three parameters are used to characterize the performance of an EQ circuit, CF, RUH, and RUS, as shown in Fig. 4(d). The CF specifies the frequency point when the EQ frequency response rolls up by 3 dB, which should be set as equal to $f_{-3\mathrm{dB}}$ of the channel under compensation. The RUH describes the gain difference in frequency response between the roll-up peak and low-frequency range. The RUS is the slope of the roll-up curve and should be set variably based on the ROS of the channel. Depending on the channel features, the three parameters need to be properly optimized to extend the channel bandwidth without causing over- or under-shooting.

B. Receiver Front-End Circuit (RX)

The data signal extracted from the demodulation circuit generally features a distance-dependent narrow spectrum and unavoidably consists of some carrier wave component. Therefore, the RX circuit needs to be properly designed for variable channel bandwidth extension and carrier suppression. The basic principle of designing an EQ circuit is to create a zero in its transfer function, which provides a high-pass frequency response. The most common circuit structures to introduce zeros in EQ circuits are resistive–capacitive (RC) degeneration and inductive peaking structures. The former is capable of providing a smooth and variable CF, RUS, and RUH, but at the cost of suppressing the intensity of low-frequency gain, which reduces the signal-to-noise ratio. The latter has the advantages of a higher CF and easy implementation, but unavoidably leads to over- and under-shooting in the time response. In addition, the CF and RUH cannot be tuned separately in inductance peaking structures. Here, targeting variable CF, RUS, and RUH, we choose to use the RC degeneration active EQ structure.

As shown in Fig. 5(a), the proposed RX circuit is composed of a pre-amplifier (pre-Amp) and a three-stage cascaded active EQ. The pre-Amp amplifies the demodulated signal to provide enough amplitude gain for equalization. Each EQ stage consists of two sections, an RC degeneration equalization section (shown in the red box) and a gain section (shown in the blue box) to compensate for the loss in the signal's low-frequency component during equalization process. A low-pass filter with a 1.5-MHz 3-dB bandwidth is implemented at the pre-Amp to suppress the carrier wave component and to keep the circuit stable [23]. The 1.5-MHz cut-off frequency is three times higher than the channel bandwidth and has little effect on the data signal spectrum.

The cascade EQ consists of three stages, EQ_1, EQ_2, and EQ_3, as shown in Fig. 5(a). EQ_1 is a simple first-order equalizer with R_{eq11} and C_{eq11} in parallel to introduce a single zero into the EQ section. The transfer function is shown in the following equation:

$$H_{\mathrm{EQ1}}(j\omega) = \frac{R_{\mathrm{eq13}} + R_{\mathrm{eq14}}}{R_{\mathrm{eq14}}} \cdot \frac{R_{\mathrm{eq12}}}{R_{\mathrm{eq11}} + R_{\mathrm{eq12}}} \cdot \frac{1 + j\omega C_{\mathrm{eq11}} R_{\mathrm{eq11}}}{1 + j\omega C_{\mathrm{eq11}} (R_{\mathrm{eq11}} // R_{\mathrm{eq12}})}. \quad (11)$$

The first term in (11) determines the amplification of the gain section and the second term determines the suppression of the low-frequency component. The third term contains a zero at

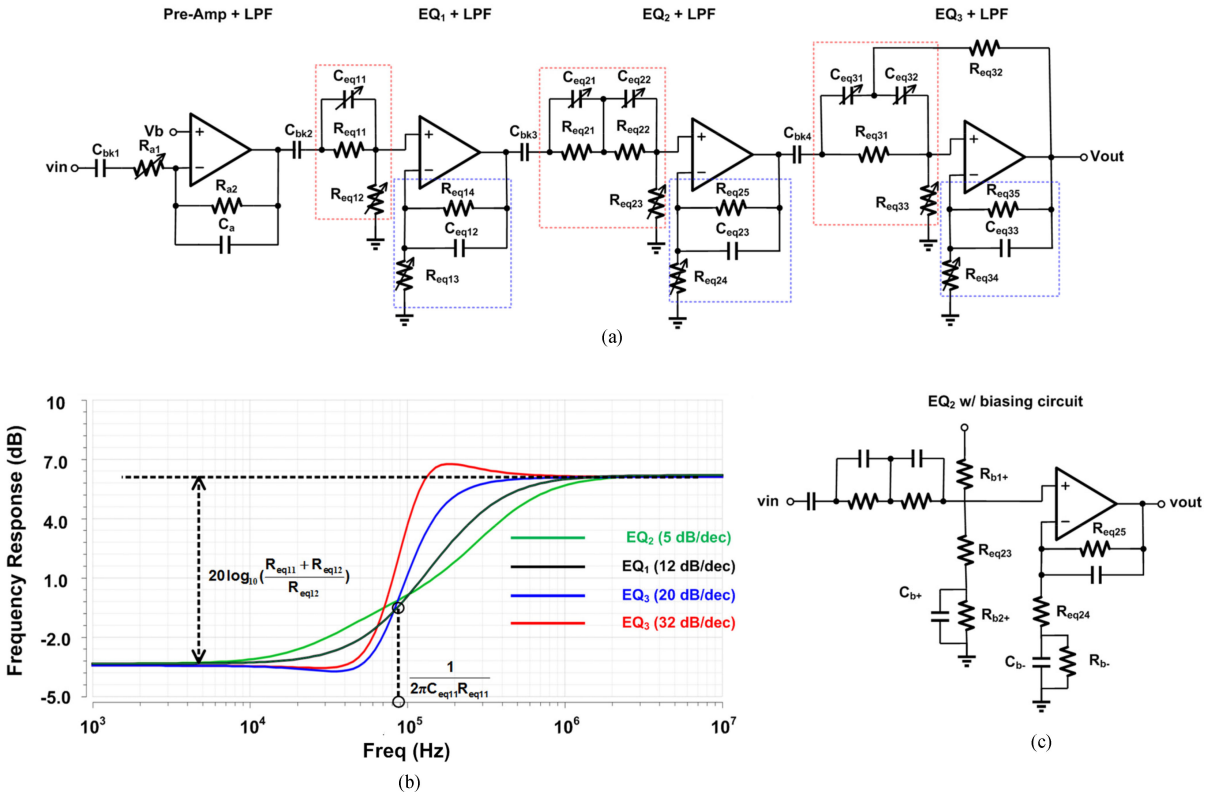

Fig. 5. (a) Schematic of the RX circuit. (b) Simulated frequency response of each EQ stage. (c) Biasing method of EQ_2.

$1/2\pi C_{eq11}R_{eq11}$, which determines the CF. The transfer function indicates that the RUH and CF can be controlled separately by tuning R_{eq12} and C_{eq11}. The first-order equalizer can theoretically provide around a 20-dB/dec RUS when frequency is higher than CF, but the initial RUS around CF is actually much less than 20 dB/dec. As a result, the actual simulated RUS of EQ_1 is 12 dB/dec for a 9.54-dB RUH as shown in Fig. 5(b).

The slow roll-up feature around the CF is exploited in EQ_2, which is still a first-order EQ but consists of two zeros introduced by C_{eq21}, R_{eq21} and C_{eq22}, R_{eq22}. By changing the separation between the frequencies of the two zeros, a variable smooth RUS can be generated within 12 dB/dec. A slow roll-up frequency response of EQ_2 with a 5-dB/dec RUS is obtained in simulation and shown with the green curve in Fig. 5(c). The transfer function of EQ_2 is presented in (12) shown at the bottom of this page.

By cascading EQ_1 and EQ_2, a wide range of the RUS, from 5–24 dB/dec can be covered by tuning the frequencies of the three zeros. However, the slow initial RUS around the CF significantly limits the compensation performance when a higher RUS is necessary. Therefore, a second-order equalizer EQ_3 is cascaded to provide a variable RUS from 20 to 32 dB/dec. The equalization section of EQ_3 is still based on the RC degeneration structure but a positive voltage feedback is applied through R_{eq32} to introduce an extra zero into the transfer function, which effectively increases the RUS. To ensure stability, the gain of EQ_3 is kept below 1.5. Variable RUS can be achieved by properly setting the values of the two capacitors C_{eq31} and C_{eq32}. The transfer function is shown in (13) at the bottom of this page, where g denotes the gain provided by the gain section of EQ_3. The simulated two different frequency responses are plotted with blue and red curve in Fig. 5(b) using different sets of degeneration capacitors C_{eq31} and C_{eq32}, as shown in Table I.

The biasing method is shown in Fig. 5(c) using EQ_2 as an example. R_{b1+}, R_{b2+}, and R_{b-} are selected to be equal and

$$H_{EQ2}(j\omega) = \frac{R_{eq24}+R_{eq25}}{R_{eq24}} \times \frac{R_{eq23}(1+j\omega R_{eq21}C_{eq21})(1+j\omega R_{eq22}C_{eq22})}{(R_{eq21}+R_{eq22}+R_{eq23})+j\omega(R_{eq22}R_{eq21}C_{eq21}+R_{eq21}R_{eq22}C_{eq22}+R_{eq23}R_{eq21}C_{eq21} +R_{eq23}R_{eq22}C_{eq22})-\omega^2 R_{eq21}R_{eq22}R_{eq23}C_{eq21}C_{eq22}} \tag{12}$$

$$H_{EQ3}(j\omega) = \frac{g\cdot(R_{eq33}+j\omega R_{eq32}R_{eq33}(C_{eq31}+j\omega C_{eq32})-\omega^2 R_{eq31}R_{eq32}R_{eq33}C_{eq31}C_{eq32})}{R_{eq31}+R_{eq32}+j\omega R_{eq31}R_{eq32}(C_{eq31}+C_{eq32})+j\omega R_{eq32}R_{eq33}(C_{eq31}+C_{eq32}) +j\omega R_{eq31}R_{eq33}C_{eq32}(1-g)-\omega^2 R_{eq13}R_{eq32}R_{eq33}C_{eq31}C_{eq32}} \tag{13}$$

TABLE I
COMPONENT PARAMETERS FOR RX CIRCUIT

Parameters	Values	Parameters	Values
Req11	10 kΩ	Ceq22	1 nF
Req12	5 kΩ	Req31	10 kΩ
Req13	5 kΩ	Req32	3.5 kΩ
Req14	5 kΩ	Req33	5 kΩ
Ceq11	200 pF	Req34	5 kΩ
Req21	5 kΩ	Req35	5.3 kΩ
Req22	5 kΩ	Ceq31[a]	400 pF
Req23	5 kΩ	Ceq32[a]	400 pF
Req24	5 kΩ	Ceq31[b]	275 pF
Req25	5 kΩ	Ceq32[b]	580 pF
Ceq21	160 pF		

[a]Capacitor values for generating 32-dB/dec RUS.
[b]Capacitor values for generating 20-dB/dec RUS.

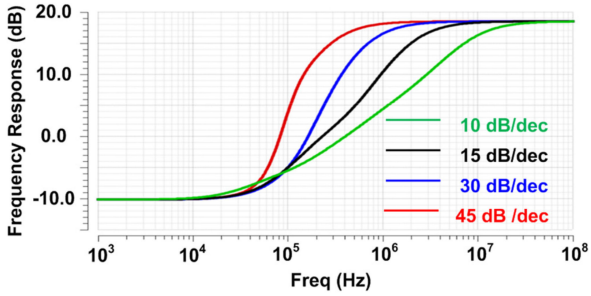

Fig. 6. Simulated frequency response of the entire three-stage EQ.

much larger than R_{eq23}, R_{eq24}, and R_{eq25}. Therefore, the bias voltages at the core amplifier input and output nodes are fixed to half of the supply voltage. A capacitive coupling method is used between each stage in the RX circuit to isolate the dc bias of each circuit stage.

The entire EQ circuit is capable of providing a wide RUS tuning range from 10 to 45 dB/dec, as shown in Fig. 6. The CF and RUH can be variably set by the proper selection of degeneration capacitors and resistors. With a 6 V voltage supply from a power management circuit connected with the power filter, the RX circuit consumes a power of 30 mW. All simulation parameters for the EQ circuit are summarized in Table I.

IV. DESIGN OF THE MWPDT SYSTEM

A. System Overview

To verify the performance of the proposed RX circuit, an MWPDT system is designed, as shown in Fig. 7. A series–series capacitive matched two-coil structure with a resonance frequency f_c at 4.25 MHz is employed for a shared power and data transfer channel. The amplitude-shift-keying (ASK) modulation scheme is adopted here to simplify the receiver design. Compared with other modulation schemes such as frequency-shift-keying and phase-shift-keying, the ASK modulated data can be recovered on the receiver side using only passive components such as rectification diodes and cascaded filters, which gets rid of active circuits such as mixers and local oscillators and is more suitable for low power IoT devices. The data signal from the baseband is modulated with a 4.25-MHz power carrier wave, amplified using an RF PA and then transmitted through the MWPDT channel. After rectification using a full-bridge rectifier, a PDD circuit based on cascaded filters is applied to recover the power and data signal and the RX circuit is connected in series following the PDD circuit for the variable channel compensation.

B. Power and Data Decoupling Circuit

The received signal from the receiving coil consists of three frequency components, dc power, low-frequency data signal, and high-frequency carrier wave component. A cascaded three-stage filter is applied to separate different frequency components as shown in Fig. 8(a). The normalized frequency response of each stage is calculated analytically and presented in Fig. 8(b). For power extraction, a 400-μF capacitor is connected in parallel with a standard 50-Ω load to create a low-pass filter to separate the dc power component. A second-order low-pass filter consisting of C_{df1}, R_{df1}, C_{df2}, and R_{df2} is used to extract the data signal. The small signal input impedance of the RX circuit is 5 kΩ and does not affect the performance of the filter. The frequency response of the second-order filter features a sharp out-of-band ROS and can better suppress the influence of the carrier component, as shown with the blue solid curve in Fig. 8(b). Since $R_{df1} \ll R_{\mathrm{load}}$, the data filter has very little effect on the power extraction at low frequencies. The pole of the second-order filter is set to 1 MHz, which is over two times higher than the channel bandwidth under testing and does not affect the high-speed data extraction. The extracted data signal across C_{df2} will be fed into the RX circuit for further processing. A small inductor is connected in parallel to suppress the effect of the carrier on power and data extraction. The transfer functions of the power, data and carrier filters are shown in (14)–(16) at the bottom of this page. All component parameters used in the design are shown in Table II.

$$H_{\mathrm{power}}(j\omega) = \frac{R_{\mathrm{load}}(1+j\omega C_{df1}R_{df1})}{R_{\mathrm{load}}(1+j\omega C_{df1}R_{df1}) + R_{df1}(1+j\omega C_{pf}R_{\mathrm{load}}) + j\omega L_f(1+j\omega C_{df1}R_{df1})(1+j\omega C_{pf}R_{\mathrm{load}})} \tag{14}$$

$$H_{\mathrm{data}}(j\omega) = \frac{R_{df1}\frac{1+j\omega C_{pf}R_{\mathrm{load}}}{1+j\omega C_{df2}R_{df2}}}{R_{\mathrm{load}}(1+j\omega C_{df1}R_{df1}) + R_{df1}(1+j\omega C_{pf}R_{\mathrm{load}}) + j\omega L_f(1+j\omega C_{df1}R_{df1})(1+j\omega C_{pf}R_{\mathrm{load}})} \tag{15}$$

$$H_{\mathrm{carrier}}(j\omega) = \frac{j\omega L_f(1+j\omega C_{df1}R_{df1})(1+j\omega C_{pf}R_{\mathrm{load}})}{R_{\mathrm{load}}(1+j\omega C_{df1}R_{df1}) + R_{df1}(1+j\omega C_{pf}R_{\mathrm{load}}) + j\omega L_f(1+j\omega C_{df1}R_{df1})(1+j\omega C_{pf}R_{\mathrm{load}})} \tag{16}$$

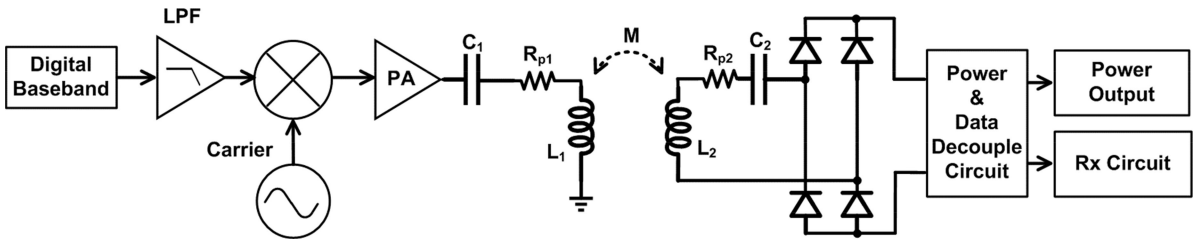

Fig. 7. Block diagram of the designed MWPDT system.

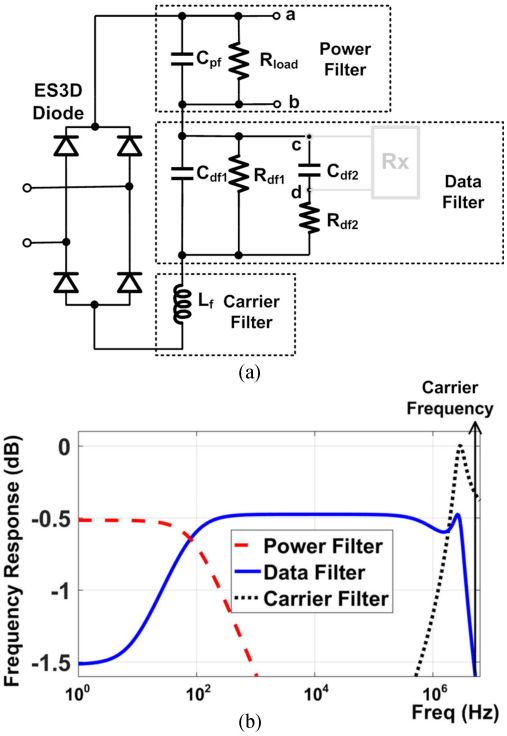

Fig. 8. (a) Schematic of the PDD circuit. (b) Frequency response of the PDD circuit.

TABLE II
COMPONENT PARAMETERS OF MWPDT SYSTEM

Parameters	Values	Parameters	Values
Rload	50 Ω	Diode	ES3D
Cpf	400 uF	L_1	31.1 uH
Rdf1	5 Ω	R_1	14 Ω
Cdf1	31.2 nF	L_2	30.88 uH
Rdf2	50 Ω	R_2	7 Ω
Cdf2	3.12 Nf	C_1	45.1 pF
Lf	100 nH	C_2	45.41 pF

V. EXPERIMENTAL RESULTS

Fig. 9 shows the fabricated PCB for the rectifier, power management circuit, PDD circuit and RX circuit. Fig. 10 shows the complete system with a 1.5 W light emitting diode used as the load and a pseudo random binary sequence-7 (PRBS-7) used as the testing data pattern. The decoupled power and data are

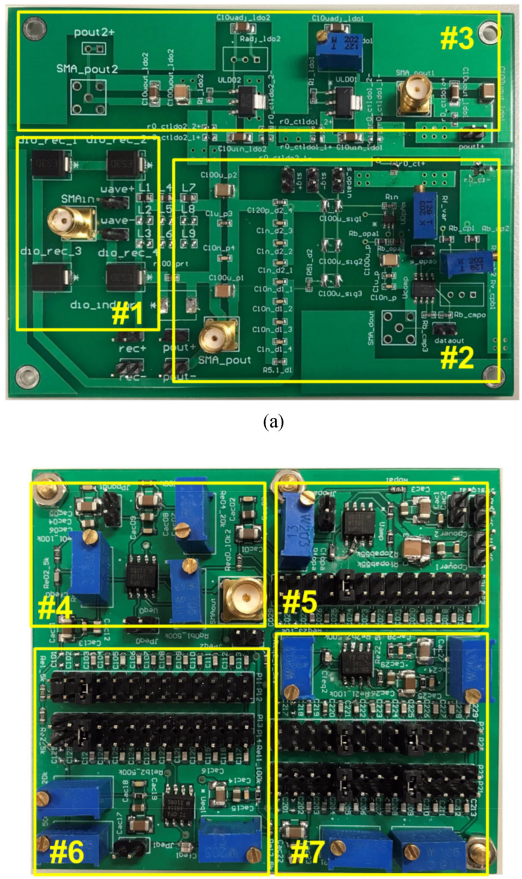

Fig. 9. (a) PCB of the full-bridge rectifier (#1), the PDD circuit (#2) and the power management circuit (#3). (b) PCB of the RX circuit, including the pre-Amp (#4), EQ_1 (#5), EQ_2 (#6), and EQ_3 (#7).

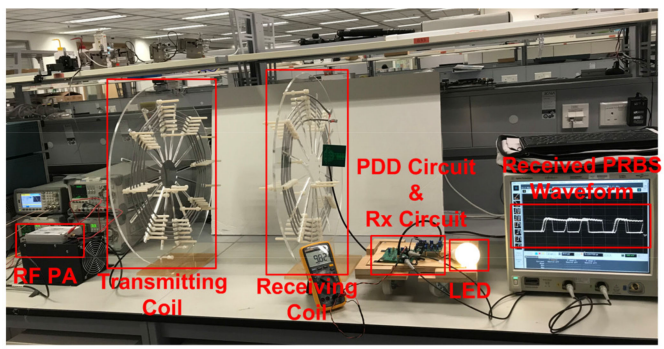

Fig. 10. Experimental setup of the complete MWPDT system.

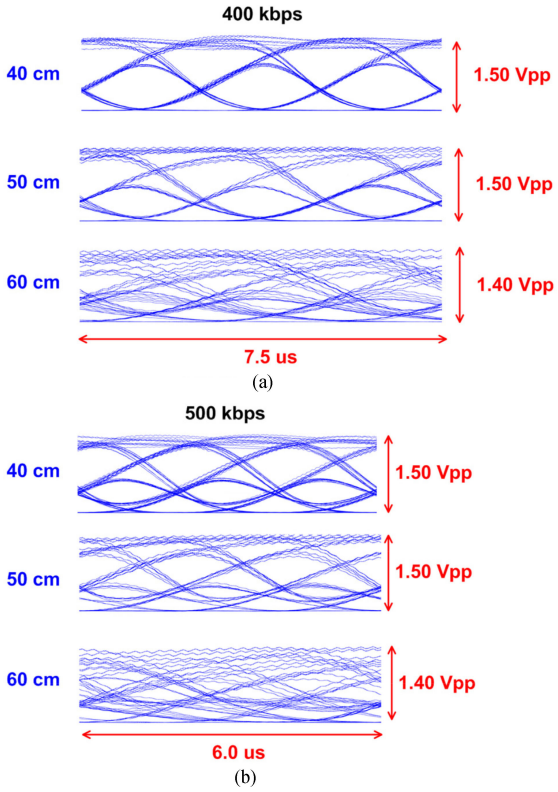

Fig. 11. (a) Eye diagrams at 400 kbps over 0.4, 0.5, and 0.6-m distances, respectively. (b) Eye diagrams at 500 kbps over 0.4, 0.5, and 0.6-m distances.

fed into the load and an oscilloscope respectively after transmission through the MWPDT system. The received waveforms are plotted into eye diagrams to directly show the data transmission quality. The radii of the coils are 0.25 m and the system is tested at 0.4, 0.5, and 0.6 m, which correspond to a *d/r* ratio of 1.4, 2.0, and 2.6, respectively. The highest transmitted power is 2 W across a 50-Ω load at 0.4 m distance. A video clip showing the complete experimental setup and demonstrating the received data waveform with and without RX circuit is also included in the supplementary material.

First, we show the variation of data transmission quality with transmission distances. Eye diagram is a common tool for evaluating the quality of received data signal, which is generated by repetitively overlapping the data patterns of PRBS-7 within 3-bit time. The eye diagrams (Eye) can be plotted from data signal (V_{data}) using the following equation:

$$\mathrm{Eye}\,(t) = V_{\mathrm{data}}\,(t + n \times 3T_b) \quad 0 < t < 3 \times T_b. \tag{17}$$

Here, n is any integer number no less than 0 and T_b is the bit period.

The measured eye diagrams under different distances without employing the proposed RX are presented in Fig. 11(a) and (b) for 400 and 500 kbps, respectively. At a 400-kbps data rate, the eye diagram over a 0.4-m transmission distance is still widely opened. However, the eye opening is smaller when the distance is increased to 0.5 m and become completely closed at 0.6 m. When the data rate is further increased to 500 kbps, the eye

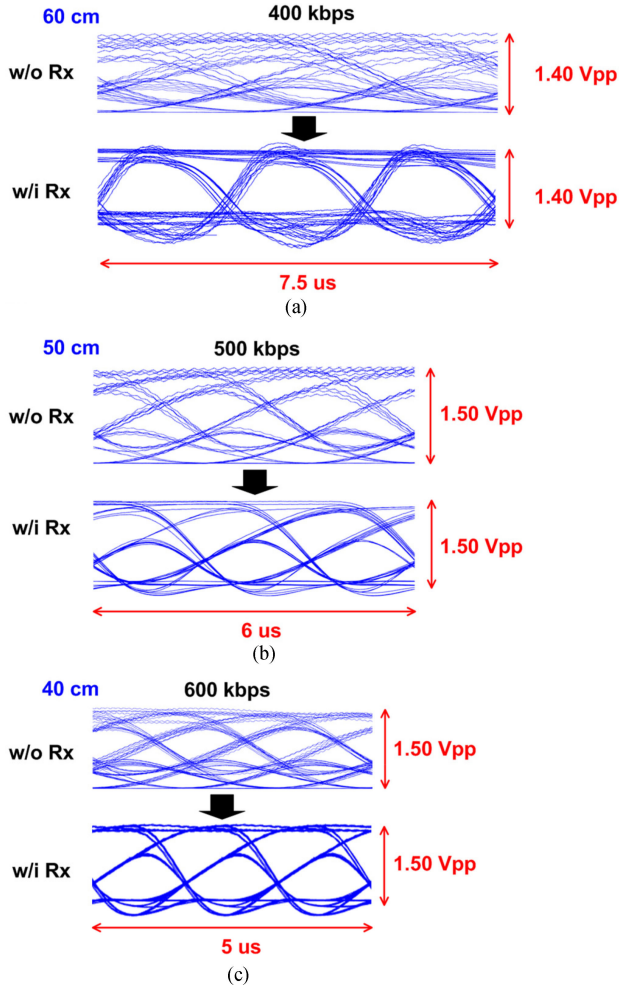

Fig. 12. (a) Eye diagrams at 400 kbps over 0.6-m distance. (b) Eye diagrams at 500 kbps over 0.5-m distance. (c) Eye diagrams at 600 kbps over 0.4-m distance.

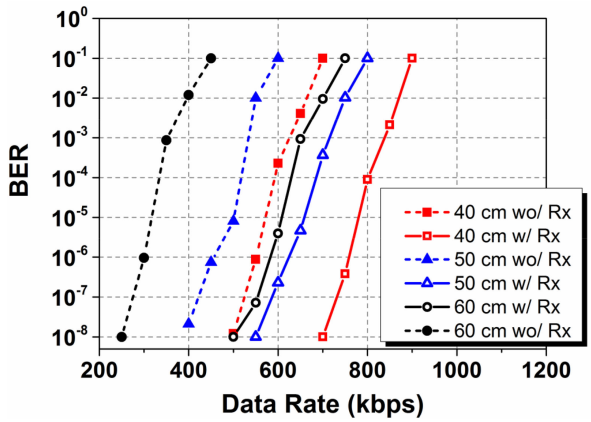

Fig. 13. BERs at different data rates under 0.4, 0.5, and 0.6-m transmission distances.

diagrams at the three distances become obviously worse compared to 400 kbps due to the limited bandwidth. Eye diagrams at both 50 and 60 cm are closed. However, by applying the proposed RX circuit to compensate for the narrow and distance-dependent bandwidth, the data transmission quality is significantly improved. The comparison of eye diagrams with and

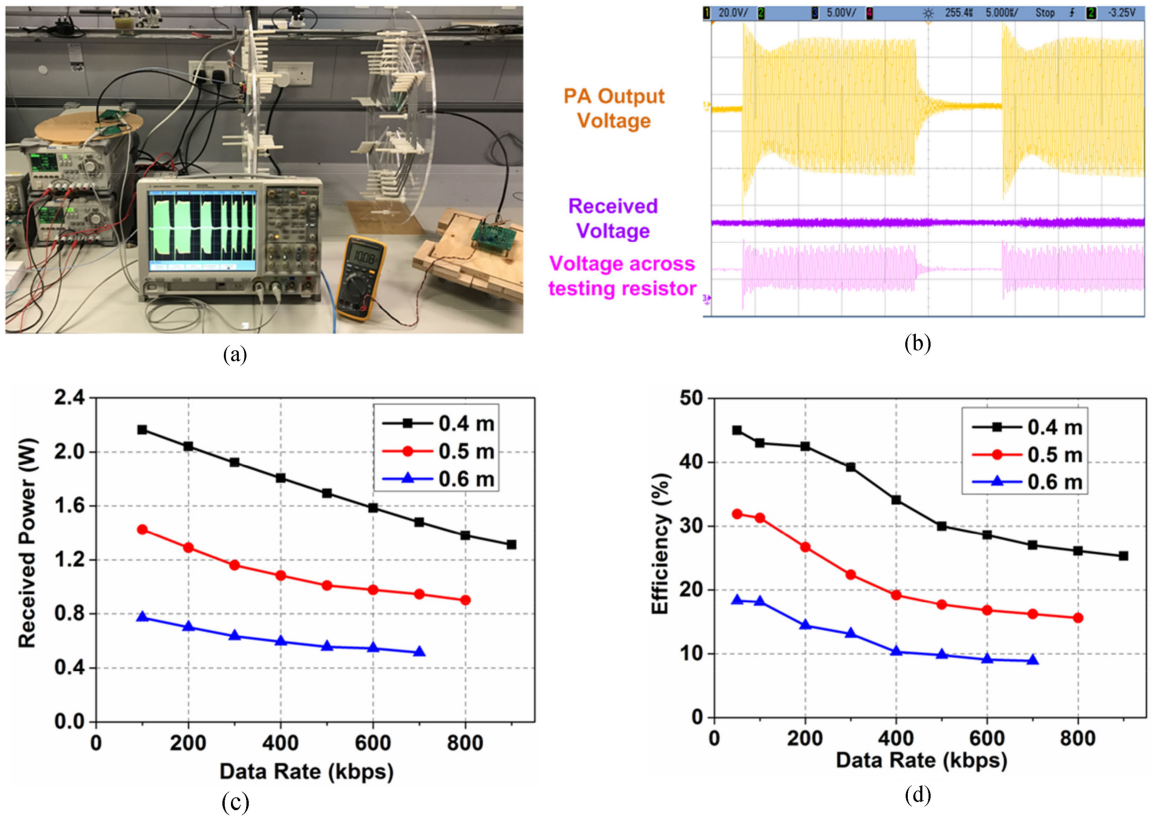

Fig. 14. (a) Measurement setup for the power transfer capacity and efficiency testing at 100 kbps over 0.4-m distance. (b) Collected waveforms of the PA output voltage at the transmitter side, received voltage across a 50-Ω load resistor and voltage across a 3.9-Ω testing resistor for calculating the PA output current. (c) and (d) measured received power and power transfer efficiency at different data rates over 0.4, 0.5, and 0.6-m distances, respectively.

TABLE III
HIGHEST DATA RATES AT DIFFERENT DISTANCES

	d = 0.4 m	d = 0.5 m	d = 0.6 m
wo/ Rx circuit	650 kbps	500 kbps	350 kbps
w/ Rx circuit	850 kbps	700 kbps	650 kbps

without the RX circuit at various distances is shown in Fig. 12. Under all these distances, the original eyes are completely closed, which means the tested data rates exceed the upper limit of the original MWPDT system. After applying the RX circuit, the recovered eye diagrams are widely opened with a sufficient signal amplitude for eyes digitizing. The measured bit error rates under different transmission distances and data rates are presented in Fig. 13. Based on the forward-error-correction limit of 3.8×10^{-3}, a highest data rate extension ratio of 85% can be achieved from 350 to 650 kbps at 0.6 m. The highest data rates of the implemented MWPDT system under different conditions with and without the RX circuit are summarized in Table III.

The power transfer capacity is measured at different data rates and distances by directly testing the received voltage across a 50-Ω resistive load, which is the typical resistance for general electronic application. Targeting at the charging and data transmission for IoT devices, the typical received power of around 2 W is measured at 100 kbps over a 0.4 m distance. The measurement setup, waveforms, and received voltage are shown in Fig. 14(a) and (b). The received power at different distances and data rates are presented in Fig. 14(c). Under each distance, the received power gradually decreases at higher data rate. The reason is that after modulating the power carrier with the data signal, the spectrum of the transmitted signal is broadened and distributes evenly around f_c. Therefore, at higher data rate, the transmitted signal spectrum partly deviates from the f_c and causes the received power to decrease. The power transfer efficiency is obtained by dividing the received power with the total transmitted power, which is calculated from the integration of the output voltage and current from the PA. Here the current is obtained by measuring the voltage across a series 3.9-Ω testing resistor on the transmitter side, as shown with light pink curve at the bottom of Fig. 14(b). The efficiency is limited to below 50% due to the fact that a 50-Ω resistor is applied at the output of the RF PA for impedance matching. The power transfer efficiencies at all three distances gradually decrease at higher data rates. The reason is that when the transmitted signal spectrum gets broadened and deviates from the center resonance frequency, the coil inductances and the matching capacitors cannot completely cancel with each other, therefore the power factor of the system drops, which leads to a higher loss on the parasitic impedance in the system.

VI. Conclusions and Discussions

This paper presents a RX circuit consists of a pre-Amp and a three-stage cascaded EQ, which is capable of providing a variable CF, RUH, and RUS to compensate for the distant-dependent MWPDT channel BW and out-of-band ROS. The three-stage cascaded EQ is composed of two first-order EQ stages and a second-order EQ stage. The proposed EQ can cover a wide RUS tuning range from 10 to 45 dB/dec. A complete MWPDT system based on a two-coil structure is built to verify the performance of the RX circuit. Experimental results demonstrate that an 85% data rate extension from 350 to 650 kbps has been achieved at a transmission distance of 0.6 m, which is 2.4 times the radii of the coils. The proposed method is also applicable to other MWPDT architectures, such as dual resonances structures and multi-coil structures, to extend the narrow channel bandwidth.

The proposed design modulates the data signal onto the power carrier and transmits the modulated wave through the single channel. This method gets rid of using an extra carrier wave for data transmission and simplifies the design to a single channel system, which is suitable for middle range operation. For short-range and high power MWPDT systems, directly modulating the data on power carrier leads to a higher signal peak to average ratio, which requires PA with larger linear range. Therefore, a dual coils or dual resonances systems can be implemented to transmit power and data simultaneously through separate channels. The proposed equalization method is still applicable to these data transmission channels to extend the communication bandwidth.

References

[1] N. Tesla, *Experiments With Alternate Currents of Very High Frequency and Their Application to Methods of Artificial Illumination*. Radford, VA, USA: Wilder, 2008.

[2] T. C. Martin and N. Tesla, *The Inventions, Researches and Writings of Nikola Tesla With Special Reference to His Work in Polyphase Currents and High Potential Lighting*. New York, NY, USA: Elect. Eng., 1894.

[3] X. Wei, Z. Wang, and H. Dai, "A critical review of wireless power transfer via strongly coupled magnetic resonances," *Energies*, vol. 7, no. 7, pp. 4316–4341, Jul. 2014.

[4] S. Y. R. Hui, W. Zhong, and C. K. Lee, "A critical review of recent progress in mid-range wireless power transfer," *IEEE Trans. Power Electron.*, vol. 29, no. 9, pp. 500–4511, Mar. 2013.

[5] A. P. Sample, D. T. Meyer, and J. R. Smith, "Analysis, experimental results, and range adaptation of magnetically coupled resonators for wireless power transfer," *IEEE Trans. Ind. Electron.*, vol. 58, no. 2, pp. 544–554, Mar. 2010.

[6] S. Li and C. C. Mi, "Wireless power transfer for electric vehicle applications," *IEEE J. Emerg. Sel. Topics Circuits Syst.*, vol. 3, no. 1, pp. 4–17, Apr. 2014.

[7] X. Li, X. Meng, C. Y. Tsui, and W. H. Ki, "Reconfigurable resonant regulating rectifier with primary equalization for extended coupling-and loading-range in bio-implant wireless power transfer," *IEEE Trans. Biomed. Circuits Syst.*, vol. 9, no. 6, pp. 875–884, Dec. 2015.

[8] S. Raju, R. Wu, M. Chan, and P. Yue, "Modeling of mutual coupling between planar inductors in wireless power applications," *IEEE Trans. Power Electron.*, vol. 29, no. 1, pp. 481–490, Jan. 2014.

[9] Y. J. Lin, H. A. Latchman, M. Lee, and S. Katar, "A power line communication network infrastructure for the smart home," *IEEE Wireless Commun.*, vol. 9, no. 6, pp. 104–111. Dec. 2002.

[10] Y. Sun, P. X. Yan, Z. H. Wang, and Y. Y. Luan, "The parallel transmission of power and data with the shared channel for an inductive power transfer system," *IEEE Trans. Power Electron.*, vol. 31, no. 8, pp. 5495–5502, Nov. 2015.

[11] L. Ji, L. Wang, C. Liao, and S. Li, "Simultaneous wireless power and bidirectional information transmission with a single-coil, dual-resonant structure," *IEEE Trans. Ind. Electron*, vol. 66, no. 5, pp. 4013–4022, May 2019.

[12] J. Wu, C. Zhao, Z. Lin, J. Du, Y. Hu, and X. He, "Wireless power and data transfer via a common inductive link using frequency division multiplexing," *IEEE Trans. Ind. Electron.*, vol. 62, no. 12, pp. 7810–7820, Jul. 2015.

[13] J. Hirai, T. W. Kim, and A. Kawamura, "Study on intelligent battery charging using inductive transmission of power and information," *IEEE Trans. Power Electron.*, vol. 15, no. 2, pp. 335–345, Mar. 2000.

[14] Y. Yao, Y. Wang, X. Liu, H. Cheng, M. Liu, and D. Xu, "Analysis, design and implementation of a wireless power and data transmission system using capacitive coupling and double-sided LCC compensation topology," *IEEE Trans. Ind. Appl.*, vol. 55, no. 1, pp. 541–551, Jan./Feb. 2019.

[15] X. Li, H. Wang, and X. Dai, "A power and data decoupled transmission method for wireless power transfer systems via a shared inductive link," *Energies*, vol. 11, no. 8, Jul. 2018, Art. no. 2161.

[16] G. Wang, P. Wang, Y. Tang, and W. Liu, "Analysis of dual band power and data telemetry for biomedical implants," *IEEE Trans. Biomed. Circuits Syst.*, vol. 6, no. 3, pp. 208–215, Jun. 2012.

[17] G. Simard, M. Sawan, and D. Massicotte, "High-speed OQPSK and efficient power transfer through inductive link for biomedical implants," *IEEE Trans. Biomed. Circuits Syst.*, vol. 4, no. 3, pp. 192–200, Jun. 2010.

[18] C. C. Huang, C. L. Lin, and Y. K. Wu, "Simultaneous wireless power/data transfer for electric vehicle charging," *IEEE Trans. Ind. Electron.*, vol. 64, no. 1, pp. 682–690, Sep. 2016.

[19] Z. Yan, L. Wu, and W. Baoyun, "High-efficiency coupling-insensitive wireless power and information transmission based on the phase-shifted control," *IEEE Trans. Power Electron.*, vol. 33, no. 9, pp. 7821–7831, Nov. 2017.

[20] J. O. Mur-Miranda *et al.*, "Wireless power transfer using weakly coupled magnetostatic resonators," in *Proc. Energy Convers. Congr. Expo.*, 2010, pp. 4179–4186.

[21] T. Imura and Y. Hori, "Maximizing air gap and efficiency of magentic resonant coupling for wireless power transfer using equivalent circuit and Neumann formula," *IEEE Trans. Ind. Electron.*, vol. 58, no. 10, pp. 4746–4752, Oct. 2011.

[22] J. Sun and K. J. Karimi, "Small-signal input impedance modeling of line-frequency rectifiers," *IEEE Trans. Aerosp. Electron. Syst.*, vol. 44, no. 4, pp. 1489–1497, Oct. 2008.

[23] Aug. 2014. [Online]. Available: http://www.ti.com/product/OPA1611

Li Wang (S'17) received the bachelor's degree from the Huazhong University of Science and Technology, Wuhan, China, in 2016, majoring in microelectronics. He is currently working toward the Ph.D. degree at the Department of Electronic and Computer Engineering, Hong Kong University of Science and Technology, Hong Kong.

Xianbo Li (S'15–M'17) received the bachelor's degree in microelectronics from Sun Yat-sen University, Guangzhou, China, in 2010, and the master's degree in microelectronics and solid-state electronics from South China University of Technology, Guangzhou, in 2013, and the Ph.D. degree in electronic and computer engineering from Hong Kong University of Science and Technology (HKUST), Hong Kong, in 2017.

He is currently a Postdoctoral Fellow with HKUST. His research interests include system-on-chip design for optical wireless communication (including visible light communication) and multifunctional GaN micro-LED display, and circuits and systems for Internet-of-Things applications.

Salahuddin Raju (S'11–M'16) received the Ph.D. degree from the Hong Kong University of Science and Technology, Hong Kong, in 2016.

He was the Chair of HKUST IEEE Solid-State Circuit Society Student Chapter. He was a recipient of the Hong Kong Ph.D. Fellowship Scheme (HKPFS) from the Research Grants Council (RGC) of Hong Kong. His research interests include on-chip power management, integrated magnetics, packaging technology, and wireless power.

C. Patrick Yue (S'93–M'98–SM'05–F'15) received the B.S. (Hons.) degree from the University of Texas at Austin, Austin, TX, USA, in 1992, and the M.S. and Ph.D. degrees in electrical engineering from Stanford University, Stanford, CA, USA, in 1994 and 1998, respectively.

He has been a Professor with the Electronic and Computer Engineering Department, Hong Kong University of Science and Technology (HKUST), since 2010. Between 2014 and 2015, he served as the Associate Provost for Knowledge Transfer. He is also the Founding Director of the HKUST-Qualcomm Joint Innovation and Research Lab and the Center of Industry Engagement and Internship with the School of Engineering. His current research interests include system-on-a-chip design for high-speed fiber-optic communication, visible light communication, and wireless power transfer for bio-implants. He cofounded Atheros Communications (now Qualcomm-Atheros), in 1998. While working in Silicon Valley, he served as a Consulting Assistant Professor at Stanford. In 2003, he joined Carnegie Mellon University as an Assistant Professor, and in 2006 he moved to the University of California Santa Barbara and was promoted to Professor in 2010. He has contributed to more than 130 peer-reviewed papers, 2 book chapters, and holds 14 U.S. patents.

Prof. Yue has served on the committees of IEEE Symposium on VLSI Circuits (VLSI-Circuits), IEEE European Solid-State Circuits Conference (ESSCIRC), IEEE MTT-S International Wireless Symposium (IWS), IEEE RFIC Symposium (RFIC), IEEE Asian Solid-State Circuits Conference (A-SSCC) and other IEEE-sponsored conferences. He was an Editor of the *IEEE Electron Device Letters* and *IEEE Solid-State Circuit Society Magazine*. He was a co-recipient of the 2003 International Solid-State Circuits Conference (ISSCC) Best Student Paper Award and the 2016 IEEE International Wireless Symposium Best Student Paper Award. He is an elected AdCom Member of the IEEE Solid-State Circuit Society. In 2016, he received the 11th Guanghua Engineering Science and Technology Youth Award by the Chinese Academy of Engineering (CAE). He is a Senior Member of Optical Society of America.